# DIII-D contributions towards the scientific basis for sustained burning plasmas

## C.M. Greenfield and the DIII-D Team

General Atomics, PO Box 85608, San Diego, CA 92186-5608, USA

## Abstract

DIII-D is making significant contributions to a scientific basis for sustained burning plasma operation. These include explorations of increasingly reactor-relevant scenarios, studies of key issues for projecting performance, development of techniques for handling heat and particle efflux, and assessment of key issues for the ITER research plan. Advanced scenarios are being optimized in DIII-D via experiments to empirically determine the relationship between transport and the current profile, which in turn can provide essential input to inform improvement of the theory-based models that do not currently capture the observed behaviour. Joint DIII-D/JET $\rho^*$ scans in the hybrid regime imply Bohm-like confinement scaling. Startup and shutdown techniques were developed for the restrictive environment of future devices while retaining compatibility with advanced scenarios. Towards the goal of a fully predictive capability, the DIII-D program emphasizes validation of physics-based models, facilitated by a number of new and upgraded diagnostics. Specific areas include transport, rotation, energetic particles and the H-mode pedestal, but this approach permeates the entire research programme. Concerns for heat and particle efflux in future devices are addressed through studies of ELM control, disruption avoidance and mitigation, and hydrogenic retention in DIII-D's carbon wall. DIII-D continues to respond to specific needs for ITER. Recent studies have compared H-mode access in several different ion species, identifying not only isotopic, but density, rotation and geometrical dependences that may guide access to H-mode during ITER's non-activated early operation. DIII-D used an insertable module to simulate the magnetic perturbations introduced by one of ITER's three test blanket module sets, demonstrating that little impact on performance is seen at ITER equivalent levels of magnetic perturbation.

(Some figures in this article are in colour only in the electronic version)

## 1. Introduction

DIII-D research is contributing to the scientific basis for the optimization of the tokamak approach to fusion energy production. Ensuring the success of ITER remains a major priority of the programme, as its needs evolve from specific short-term design issues towards longer term concerns for ITER research planning. For longer term success of ITER, and indeed of future devices up to and including a power plant, DIII-D research works towards scientific understanding across a range of research areas. The results of these endeavours will be embodied in reliable predictive tools that can be applied towards design of devices and experiments.

In this paper, we will summarize recent research contributing to these goals. DIII-D research continues to advance development, characterization and access to operating scenarios of interest and importance for burning plasmas (section 2). Relying on DIII-D's comprehensive set of control tools and diagnostics, a vigorous research programme is underway to carry out specific tests of physics-based models of transport, rotation, energetic particle (EP) effects and the H-mode pedestal (section 3). Methods for handling heat

and particle efflux, including transients (edge localized modes (ELMs) and disruptions) and tritium retention, are described in section 4. DIII-D continues to be responsive to the specific needs of ITER. Two of these needs, isotope dependence of the L–H threshold and the plasma response to test blanket modules (TBMs), are described in section 5. In section 6, we will briefly discuss new capabilities being added to DIII-D and the future research directions that will be enabled.

## 2. Scenario development, characterization and access

### 2.1. High-beta steady-state scenario optimization

Steady-state tokamak operation requires that 100% of the plasma current be driven non-inductively ($f_{NI} = 1$). This current is supplied in part by a combination of externally applied sources. In DIII-D, these often include electron cyclotron current drive (ECCD) [1] and neutral beam current drive (NBCD) [2]. It is desirable to minimize the requirement for external current drive for reasons of cost and recirculating power. Fortunately, high-performance fusion plasmas can
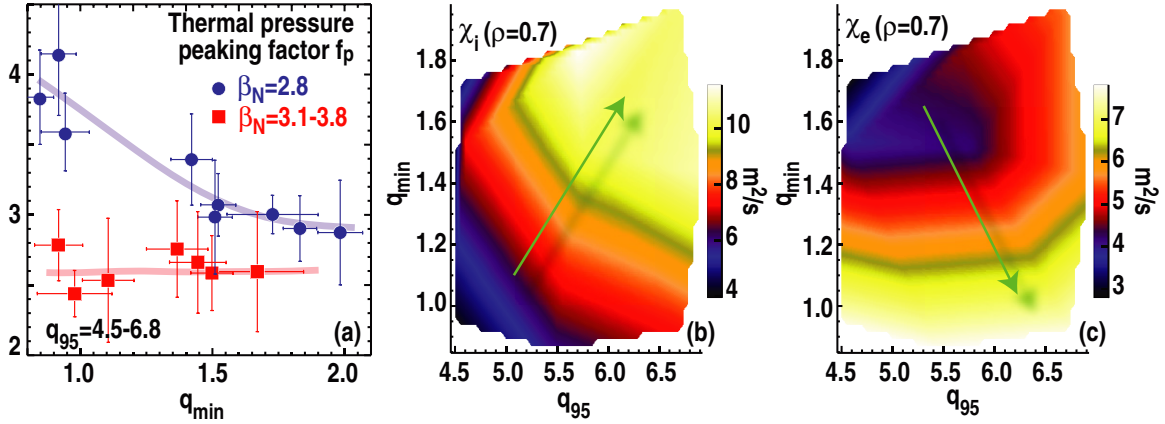
**Figure 1.** (*a*) The thermal pressure peaking factor in steady-state scenario discharges decreases with increasing $q_{min}$ and $\beta_N$. The circular symbols are from a set of discharges with NBI controlled to maintain $\beta_N \approx 2.8$. The discharges shown with square symbols are heated by the maximum available power $P_{NBI} = 13.5$ MW, with the resulting $\beta_N$ depending on confinement. The observed behaviour is a consequence of variations in ion (*b*) and electron (*c*) thermal diffusivity, whose variation differs from model-based predictions.

provide a large fraction of the current through self-driven bootstrap current [3]. In a global sense, the fraction of current driven by bootstrap increases as

$$f_{BS} \propto q \beta_N f_P, \qquad (1)$$

where $q$ is the plasma safety factor, $\beta_N$ is the normalized plasma beta and $f_P = (n_e(0)T_e(0) + n_i(0)T_i(0))/\langle n_e T_e + n_i T_i \rangle$ is the thermal pressure peaking factor. The apparent simplicity of this relation, however, is deceiving, since $f_P$ is strongly coupled to both $q$ and $\beta_N$ via transport behaviour that is not fully captured by existing transport models.

To experimentally optimize the $q$ profile for discharges in DIII-D with 100% of the current driven non-inductively ($f_{NI} = 1$), the self-consistent response of the plasma profiles to changes in the $q$ profile was studied in high-$f_{NI}$, high-$\beta_N$ discharges [4, 5]. In discharges where the heating power (neutral beams) is regulated to maintain $\beta_N = 2.8$ (blue circles in figure 1(*a*)), the pressure profile peaking decreases (profile flattens) with increasing $q_{min}$. Also shown (red squares) are points from a set of discharges where the heating power was fixed at $P_{NBI} = 13.5$ MW, so that $\beta_N$ varied between 3.1 and 3.8. None of these discharges reached an MHD stability limit; they were all limited in performance by transport. In these discharges, the variation of profile shape with $q_{min}$ was absent, and $f_P$ remained at a lower value than seen at $\beta_N = 2.8$. Referring back to equation (1), we conclude as follows:

- at fixed $\beta_N$, $f_P$ decreases with increasing $q_{min}$;
- at fixed $q_{min}$, $f_P$ decreases with increasing $\beta_N$.

As might be expected from this behaviour, thermal transport varies significantly as the current profile is varied. Several observations can be made from ion (figure 1(*b*)) and electron (figure 1(*c*)) thermal diffusivities, determined from power balance analysis of this dataset. First, the transport in both channels varies strongly with the current profile. Second, the electrons and ions do not respond in the same way. Modelling of these cases with a trapped gyro-Landau fluid code (TGLF) [6] show that variations in the linear growth rate do not correlate well with the observed transport changes [7].

The broadening of the pressure profile at high $\beta$ results in a bootstrap current density profile that is relatively flat between the axis and the H-mode pedestal. Therefore, significant externally driven current is required in the region inside the H-mode pedestal to match the profiles of the non-inductive current density ($J_{NI}$) to the desired total current density ($J$). In these experiments, the profiles of $J_{NI}$ and $J$ were most similar at $q_{min} \approx 1.35$–1.65, $q_{95} \approx 6.8$, where $f_{BS}$ is also maximum, establishing this $q$ profile as the most optimal choice for $f_{NI} = 1$ operation in DIII-D with the existing set of external current drive sources.

These experiments focused on establishing the desired conditions for a sustained scenario, but not on actual sustainment. This will require replacement of inductively driven current, driven near the half-radius [8]. In the present experiments, this current is primarily provided by ECCD. Modifications now underway will make off-axis NBCD and additional ECCD available for future experiments.

Plasmas in the steady-state scenario often have $\beta_N$ above the no-wall stability limit. Recent research has identified kinetic effects as important for resistive wall mode (RWM) stability in this regime, even in non-rotating plasmas [9, 10]. Additional progress has also been made in simultaneous active control of error fields and RWMs [11].

### 2.2. Confinement in advanced inductive scenarios

Advanced inductive (AI) plasmas are a realization of the ITER hybrid scenario, providing high neutron fluence in a prolonged inductive discharge [12]. The performance improvement over conventional (ITER baseline) H-mode is usually ascribed to a broader current profile, but a complete physics basis for hybrid scenarios is a subject of continued study. This results in some uncertainty in extrapolation to ITER. DIII-D and JET [13] have recently performed a joint experiment to determine the dependence of confinement on several key parameters [14]. The largest extrapolation to ITER is in its size, expressed in dimensionless quantities as $\rho^*$, the normalized ion gyroradius evaluated at normalized radius $\rho = 0.5$. In this experiment, the two devices spanned a range of 2.7 in $\rho^*$, considerably larger than is possible in any single device and about equal
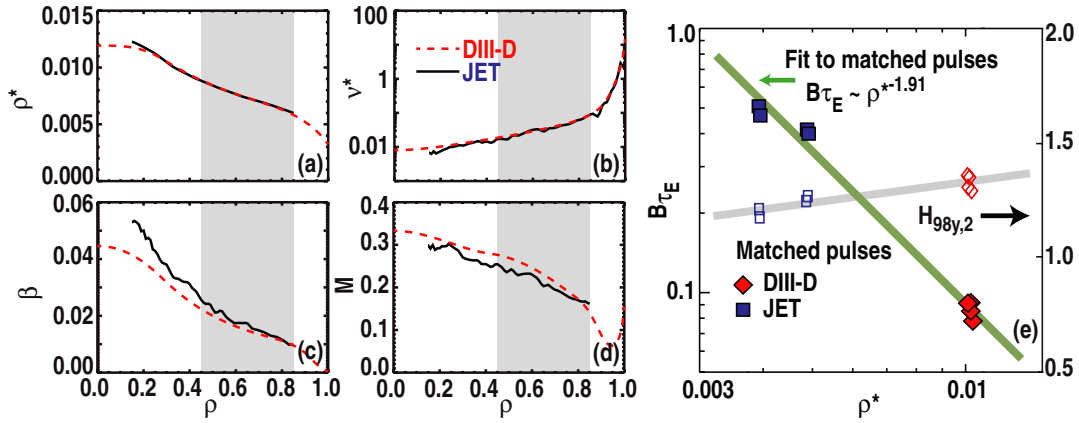
**Figure 2.** (*a*)–(*d*) 'Dimensionally identical' AI discharges in DIII-D and JET, which are controlled to match normalized gyroradius $\rho^*$, collisionality $\nu^*$, $\beta$ and Mach number $M$ in a global sense only, exhibit well-matched profiles of the same over most of the radial extent of the plasma. This indicates that the same physics governs the AI discharges in each device. (*e*) Normalized energy confinement $B\tau_E$ versus $\rho^*$ (closed symbols). The dependence on $q_{\mathrm{cyl}}$ and $\beta$, from the ITER98 ($y$, 2) scaling, is included to account for small residual variations in $q$ and $\beta$ in the data. $H_{98y,2}$ is shown by open symbols.

to the difference between JET and ITER. To carry out these experiments, plasmas with the same shape and aspect ratio were produced in both tokamaks. Linear dimensions of the plasma in JET were larger by a factor of 1.67 compared with DIII-D. As closely as possible, dimensionless parameters other than $\rho^*$ were matched globally to those expected in ITER and well matched between JET and DIII-D. Comparison of profiles of these dimensionless parameters reveals a remarkable match (figures 2(*a*)–(*d*)) in a local sense, indicating that the scenarios in the two devices are governed by the same physics.

The global energy confinement is found to behave in a roughly Bohm-like fashion (figure 2(*e*)). This result does not yet provide a sufficient basis to predict performance of AI plasmas in ITER, as the present experiments did not match all of ITER's dimensionless parameters. In particular, the collisionality was different from that expected in ITER, and there are indications that this might have a significant effect on transport behaviour [12]. These studies are continuing, with the ultimate goal of determining the dependence of confinement on all of the relevant dimensionless parameters, thereby enabling accurate extrapolation to ITER.

### 2.3. Access to and safe shutdown from ITER operating scenarios

DIII-D is developing and demonstrating startup, ramp-up and ramp-down scenarios that are compatible with ITER's restrictive environment and capable of producing appropriate target conditions for several ITER operating scenarios. Low breakdown electric fields $E$ have been achieved with ($E \approx 0.21\,\mathrm{V\,m^{-1}}$, lower than the maximum $0.3\,\mathrm{V\,m^{-1}}$ specified for ITER) and without ($E \approx 0.42\,\mathrm{V\,m^{-1}}$) assistance from electron cyclotron heating (ECH). Transitioning to a large bore divertor configuration early in the current ramp reduces heat flux to poloidal limiters, and allows control of the internal inductance $\ell_i$ by varying the current ramp rate. Efforts to model the current ramp phase with CORSICA [15], a 2D equilibrium and 1D transport predictive integrated modelling code, have successfully matched the evolution of $T_e$ and $q$ near the axis, but have so far not successfully matched the current profile, due
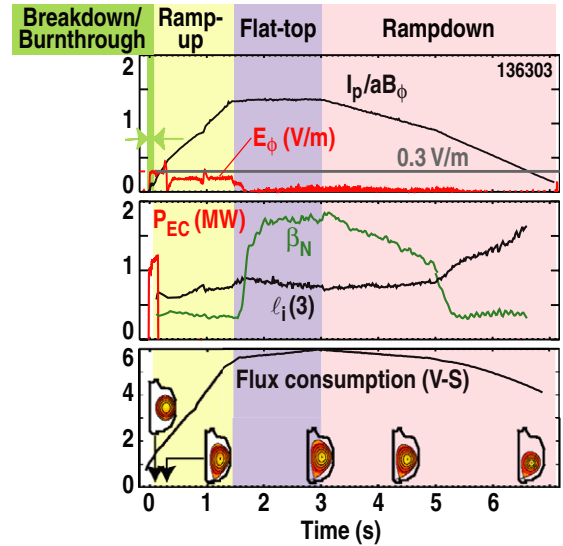


**Figure 3.** An ITER baseline scenario discharge achieved with startup, ramp-up and ramp-down scenarios optimized for the restrictions anticipated in future devices.

in part to inaccuracies in reproducing the experimental edge $T_e$ evolution in the model [16]. These ramp-up and ramp-down scenarios have been combined into a single discharge [17], with a flattop matched to the ITER baseline (conventional H-mode) scenario (figure 3). Similar demonstrations have been carried out in ohmic and hybrid scenario discharges.

DIII-D experiments have demonstrated that full ramp-down can be achieved with no additional transformer flux. We find that a controlled elongation ramp-down is effective in preventing uncontrolled density increases that might trigger a disruption. The ITER ramp-down scenario is terminated by exceeding the vertical control limit, in agreement with calculations. However, the termination occurs reproducibly below the ITER equivalent current level of 1.4 MA, where arbitrary disruptivity rates are allowed.

DIII-D discharges have been developed to simulate the remaining leading operational scenarios for ITER, and detailed modelling of these experiments is in progress [18].
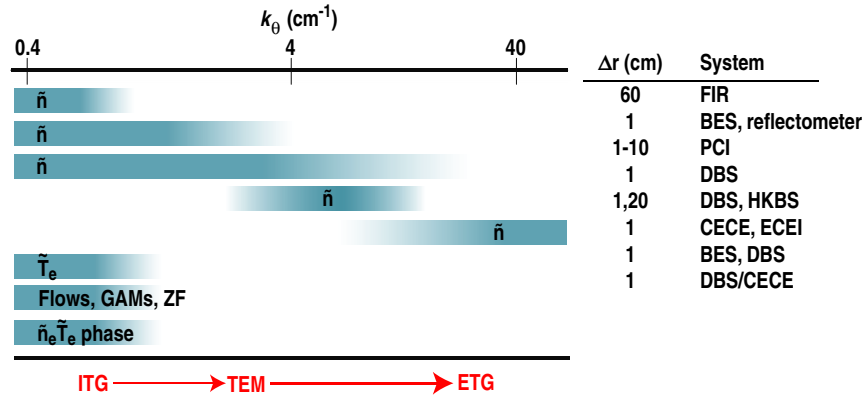
**Figure 4.** Validation studies in DIII-D take fluctuations over a wide range of spatial scales and fluctuating fields into consideration. The operative drift wave instabilities, in order of increasing $k_\theta$, are believed to be the ion temperature gradient (ITG), trapped electron mode (TEM) and electron temperature gradient (ETG) modes. The large suite of diagnostics, deployed to make many of the appropriate measurements, includes far infrared scattering (FIR), beam emission spectroscopy (BES), reflectometry, phase contrast interferometry (PCI), doppler backscattering (DBS), high-*k* backscattering (HKBS), correlation electron cyclotron emission (CECE) and electron cyclotron emission imaging (ECEI).
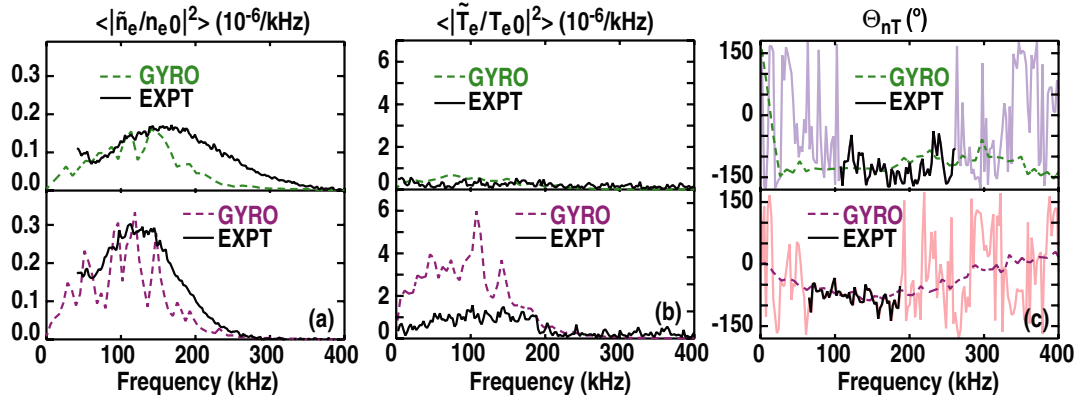


**Figure 5.** Measured (EXPT) and calculated (GYRO) fluctuation spectra at $\rho = 0.6$ with NBI-heated (upper row) discharges and those where $T_e$ is increased by 50% by adding ECH (lower row). (*a*) Low-*k* density fluctuations measured by BES; (*b*) low-*k* electron temperature fluctuations measured by CECE; (*c*) cross-phase between density and temperature fluctuations as measured by CECE and DBS (at the same location).

## 3. Improved physics basis for performance projections

### 3.1. Transport model validation

Detailed validation studies underway at DIII-D aim to test physics-based transport models in L-mode [19–21], H-mode and QH-mode [22] plasmas. 'Validation studies' here refers to a process comparing measurements with simulated values to assess the models' accuracy as important parameters are varied. Fluctuation diagnostics for multiple fields (e.g. $n_e$ and $T_e$) spanning a wide range of spatial scales ($k_\theta \rho_s \approx 0.1$ to >10; $k_\theta \approx 0.4$ to >40 cm$^{-1}$) (figure 4), and simulations (e.g. GYRO [23]) have advanced sufficiently to make such studies viable. Essential to these comparisons are synthetic diagnostics, digital analogues of real diagnostics applied to the output of the models.

One such study is a recent L-mode $T_e/T_i$ scan [19], where ECH was applied to a neutral beam injection (NBI)-heated L-mode plasma, with a resulting 50% increase in $T_e$ in the mid-core region of interest ($0.5 \leqslant \rho \leqslant 0.8$). Figure 5 shows the resulting change in measured and calculated fluctuation spectra at $\rho = 0.6$ [19]. The largest change with the additional heating is the increase in low-*k* $\tilde{T}_e/T_e$. Although the shape of the resulting fluctuation spectrum is approximately predicted by GYRO, the simulation predicts a response that is considerably larger than that observed in the experiment. Smaller changes, more closely predicted by GYRO, are seen in the density fluctuations $\tilde{n}_e/n_e$ and the cross-phase $\Theta_{nT}$.

GYRO-simulated thermal fluxes (not shown) are in qualitative agreement with experiment, with substantial, but incomplete, quantitative agreement. Recent GYRO calculations at $\rho = 0.8$ either do not converge or undergo numerical instabilities, indicating a possible need for coupled low through high-*k* multiple modes non-linear simulations; this is currently under investigation. These observations fit a general trend in DIII-D that simulated transport and fluctuation levels in the mid-core region ($\rho \approx 0.5$) are often in better agreement with experiment than those in the outer region ($\rho > 0.75$), where edge effects may be important [19]. Results such as these are noteworthy as they point to potential future research paths.
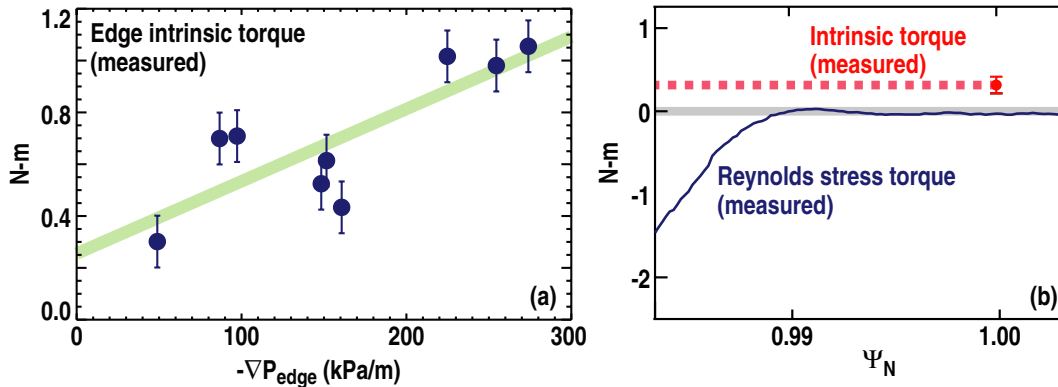
**Figure 6.** (*a*) The measured edge intrinsic torque increases with the strength of the edge pressure gradient. (*b*) The Reynolds stress torque, measured via Langmuir probes, is very small at the edge, and insufficient to be the driver behind this intrinsic torque.

### 3.2. Edge momentum source for intrinsic rotation during H-mode

Rotation has a significant, often beneficial, effect on both transport and stability in tokamak plasmas. DIII-D is working towards a predictive understanding of rotation, with recent emphasis on drive mechanisms [24]. The main source of momentum in DIII-D is neutral beams, but driving large rotation in ITER and other future tokamaks via NBI will be challenging at best.

Experiments on multiple machines over the past several years have shown that the plasma can generate its own, 'intrinsic' rotation. DIII-D experiments previously inferred an 'intrinsic torque' in the edge [25]. In order to improve the extrapolation to ITER, we have investigated the torque driving intrinsic rotation on DIII-D. We find that the intrinsic torque increases with edge pressure gradient (figure 6(*a*)). However, the turbulence-driven Reynolds stress [26] measured in the edge of H-mode discharges produces a negligible torque (figure 6(*b*)), inadequate to explain the intrinsic torque [27].

Recently, a strongly co-rotating layer has been observed with a reciprocating multi-tip Langmuir probe just inside the separatrix of H-mode discharges [28] (figure 7). The 1 cm-wide layer forms independently of injected torque less than 50 ms after an L–H transition. In pure ECH plasmas with no applied torque, the flat core rotation profile spins up over 600 ms to match the edge rotation layer's velocity ($\sim$35 km s$^{-1}$). This indicates that the layer is a cause, rather than effect, of core rotation and that viscous transport down the layer's gradient can slowly spin up the core.

Ion orbit loss has been suggested as a possible explanation for the observed behaviour. A simple orbit loss model [29] successfully reproduces the layer's profile shape, suggesting a link between these losses and formation of the layer. The toroidal–radial Reynolds stress [26] torque has also been considered, but it is essentially zero outside the layer's peak and becomes increasingly negative further inwards. It thus acts to *oppose* the spin-up of the core by transporting momentum outwards, directed up the layer's gradient, thereby acting to maintain the peaked shape over long timescales.
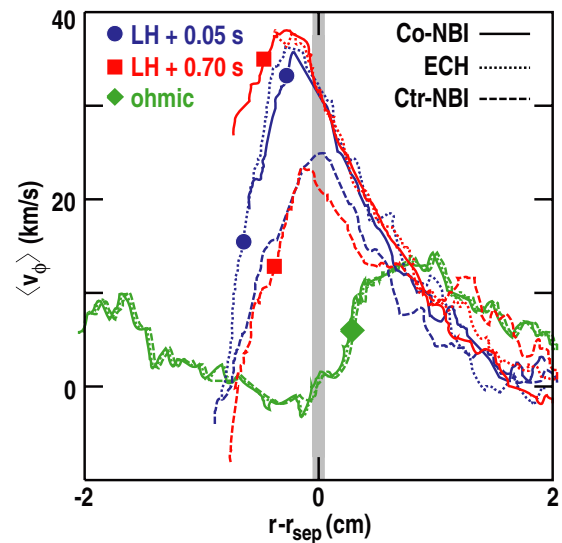


**Figure 7.** An edge co-rotation layer forms immediately after the L–H transition and is maintained for the duration of the H-mode phase. The sign of this rotation is independent of the direction of applied torque.

### 3.3. Rotation driven by dominantly non-resonant magnetic fields

In recent experiments in DIII-D, the first observation of a theoretically predicted peak in the neoclassical toroidal viscosity (NTV) torque for low toroidal rotation rates has been made [30] (figure 8). We have previously reported observations that static, dominantly non-resonant, $n = 3$ fields apply a torque to the plasma that drives it towards a counter-rotating (opposite to the plasma current) finite velocity [31]. This effect is predicted by NTV theory [32], and can be accessed through application of these fields from non-axisymmetric coils (the I-coil) in DIII-D. In the present experiment, a series of similar discharges was prepared, scanning over a range of toroidal rotation rates $\Omega$. The neutral beams are feedback controlled to maintain constant values of $\beta_N$ and $\Omega$, so that they will respond to additional torques applied by other sources. An $n = 3$ field is applied by activating the I-coil, and the NTV torque determined by the change in NBI torque required to maintain the programmed

value of $\Omega$ : $\Delta T_{NBI} = -T_{NTV}(\Omega)$. As shown in figure 8, the experimental data exhibit a peak in the torque centred at the location predicted by theory.

*3.3.1. QH-mode with zero net NBI torque.* The NTV torque can have practical benefits. QH-mode [33, 34] exhibits performance comparable to the ITER baseline ELMing H-mode, but without ELMs and their damaging effects. Its attractiveness has been limited by an operational requirement for strong NBI-driven rotation, which cannot be anticipated in ITER or any reactor grade tokamak. In recent experiments, an $n = 3$ field produced by combining the internal I- and external C-coils has been used to apply NTV torque to maintain edge rotation with zero net NBI torque [35]. In these cases, QH-mode was accessed via the usual counter-NBI technique, with the torque removed (by balancing the NBI) over about a 1 s interval. Following this, QH-mode operation with zero-net NBI torque was maintained for 1 s, until the $n = 3$ field was removed (figure 9). Previous experiments [36] have shown that sufficient rotational shear near the edge, rather than rotation itself, is needed to access the QH-mode; in these experiments
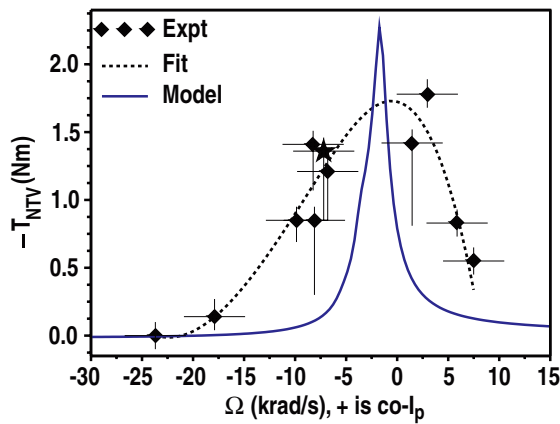
that shear is provided by NTV rather than applied NBI torque. In addition, the effect of applying predominantly non-resonant magnetic perturbations (RMPs) did not saturate at the highest perturbation amplitudes. This may open a plausible path to QH-mode utilization in ITER.

*3.4. Improved understanding of energetic particle (EP) behaviour*

Anomalous EP transport is an important, yet poorly understood, term in the power balance, making transport analysis challenging when this transport is large. This is a more serious concern for burning plasmas, where energetic $\alpha$ particles will be the primary heating source. These concerns motivate efforts to identify, understand and ultimately control this transport.

New diagnostics provide data to test models of EP instabilities and associated transport. Discrepancies between measured and theoretical EP profiles suggest that the EP population is depleted through both fine-scale turbulence and large-scale instabilities (e.g. Alfvén eigenmodes (AEs)) including toroidal AEs (TAE) and reversed shear AEs (RSAE) [37].

Two-dimensional imaging of the modes' internal structure provides unprecedented detail on the non-linear interaction of EPs with the background plasma. In a recent experiment [38], RSAEs were excited by NBI into a plasma with an off-axis minimum in the $q$ profile. Figure 10 shows a comparison of an $n = 4$ RSAE calculated by the TAE/FL [39] code (figures 10(a)–(c)) and observed via ECE imaging (figure 10(d)). The distinct poloidal shearing seen here is not reproduced by ideal MHD codes. It is reproduced by TAE/FL simulations only when coupling between the mode and the fast ion population is included (figures 10(c) and (d)), indicating that this effect may cause the shearing.

The newly commissioned DIII-D fast-ion loss detector (FILD) observes fluctuations in ion flux that are coherent at frequencies in the TAE/RSAE range (60–100 kHz) with the energy and pitch angle of lost ions; the enhanced losses occur when AE are present. When the measured pitch angle and



**Figure 8.** Comparison of measured NTV (diamonds), and cylindrical torque model (line) versus deuterium toroidal rotation rate (obtained from NCLASS) at $\rho = 0.67$. A least-squares spline fit (dashed) is shown for the data.
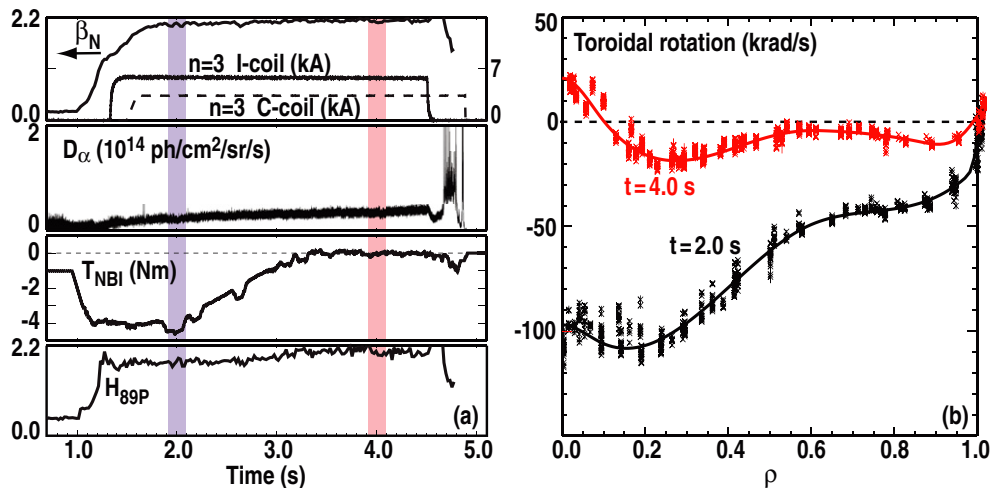


**Figure 9.** (a) $n = 3$ NTV torque is applied, via the internal I- and external C-coils, to a pre-existing QH-mode. QH-mode phase is maintained after the neutral beam driven torque is eliminated, with constant $\beta_N$ and confinement quality. (b) Toroidal rotation profiles before ($t = 2.0$ s) and after ($t = 4.0$ s) the NBI torque is removed.
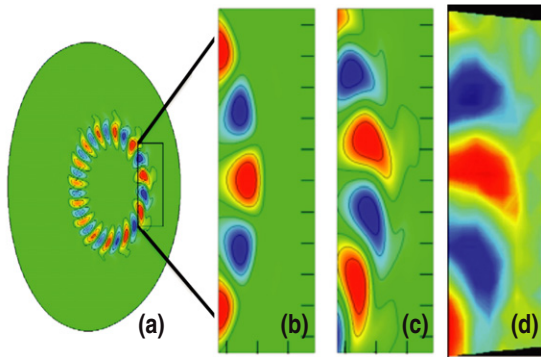
**Figure 10.** Imaging of $\tilde{T}_e/T_e$ from RSAEs. (*a*), (*b*) TAE/FL simulations; coupling between the mode and the fast ion population is not included. (*c*) The same simulation, but now including coupling between the mode and the fast ion population, displays a distinct poloidal shearing. (*d*) Measurements with ECE imaging show a similar sheared feature, indicating the importance of coupling in these simulations.

energy are used to trace backwards from the FILD aperture along a path, calculated by the ORBIT [40] code, the lost ions are found to originate from a location where AEs are known to exist (figure 11(*a*)). The FILD results, in conjunction with other measurements and calculations, allow us for the first time to directly associate fast-ion losses with AEs [37]. Figure 11(*b*) shows the spectrum of the ion flux fluctuations, indicating both TAE and RSAE frequencies are present, embedded in the fast ions striking the detector, as expected from the ORBIT calculations. The FILD also produces an image of the fluxes striking the detector. In figure 11(*c*), two features are observed. The feature on the left is identified as being associated with prompt fast-ion loss from the injected neutral beams, and is present during the entire duration of NBI. The feature on the right, however, vanishes after the TAE and RSAE activity seen in figure 11(*b*) disappears. The wealth of data available from this new diagnostic is enabling new comparisons with theory-based models of EP behaviour.

### 3.5. Predicting the H-mode pedestal

Performance predictions for ITER and other future devices are strongly dependent on the structure and magnitude of the H-mode edge pedestal. Current models are beginning to yield more consistent predictions of the pedestal characteristics. Peeling–ballooning (P–B) stability constrains the pedestal profile with the onset of ELMs, while the kinetic ballooning mode (KBM) has been proposed as a transport driving mechanism in the pedestal. These two phenomena are included in the EPED model [41], which has successfully matched observations on several tokamaks including DIII-D, JET and JT-60U. The EPED1 model, however, required an empirically determined closure relation, $\Delta_{\psi N} = c\beta_{p,ped}^{1/2}$, where $c$ is an empirically determined constant, $\Delta_{\psi N}$ is the pedestal width and $\beta_{p,ped}$ is the poloidal $\beta$ at the top of the pedestal. Recent improvements to the EPED model (EPED1.6) have eliminated this requirement by using a direct calculation of both P–B and KBM stability with no free parameters [42].

Pedestal heights measured on DIII-D, JET and C-Mod are in good agreement with the first-principles based calculation of EPED1.6 (figure 12(*a*)). Both versions of EPED give similar predictions for ITER, with a pedestal height of $\beta_{N,ped} \approx 0.6$ and width $\Delta\psi \approx 0.04$ ($\sim$4.4 cm). At the ITER reference density, and typical peaking, $\beta_{N,ped} \approx 0.6$ corresponds to $T_{ped} \approx 4.1$ keV.

As previously mentioned, the KBM is invoked as the mechanism of transport in the pedestal. Although decisive proof of the presence of the KBM in the H-mode pedestal is not in hand, observations have been made which are at least consistent with this hypothesis. Figure 12(*b*) shows BES measurements in the H-mode pedestal, exhibiting features that are expected of the KBM. In particular, we observe a large number of medium-$n$ harmonics, propagating in the ion diamagnetic direction [43].

Additional studies of the pedestal structure and its dependence on machine size scaling have been underway in joint experiments between DIII-D and JET [44, 45]. Results to date are indicative of a lack of variation of the temperature and density pedestal widths with $\rho^*$ on the two devices (figure 13). Comparison of this dataset with additional data from ASDEX Upgrade is consistent with this observation. Note that the variation seen in the DIII-D data in the density pedestal width is believed to be a consequence of neutral penetration effects and not the size scaling.

## 4. Heat and particle flux control methods

### 4.1. Reducing the impact of ELMs

The impulsive heat load from ELMs is a major concern for ITER and other next step devices. DIII-D is exploring several techniques to eliminate or mitigate ELMs, including ELM suppression by RMPs and ELM pacing by oscillating magnetic perturbation and pellet injection.

DIII-D has pioneered the use of RMPs for ELM control. When a sufficiently large current is applied to an $n = 3$ internal coil in DIII-D, ELMs are reliably and reproducibly suppressed within a particular range of safety factor (figure 14(*a*)). This effect is consistent with P–B stability calculations with the ELITE code [46] that indicate that the RMP reduces the pedestal gradient and/or current density below the P–B limit. We surmise, then, that the ELM suppression is a consequence of increased transport within the pedestal. Recent research in DIII-D is focusing on elucidating the physical causes underlying that increase, so it can be better predicted and controlled.

Upon closer examination, the non-axisymmetric fields appear to have a direct impact on particle transport, with the magnitude of the effect being dependent more on the size of the applied field than on resonant ($q$ dependent) effects (figure 15(*a*)). BES measurements indicate that changes in the RMP field have a prompt effect on fluctuations in the plasma, with the change in density occurring considerably more slowly (figure 15(*b*)) [43].

Resonant effects are, however, seen on energy transport. The electron temperature gradient (ETG) is reduced inside $\Delta q_{95}$, the range of safety factors where ELMs are suppressed (figure 16) [47]. Future experiments will focus on the physics underlying these observations.

During RMP experiments in high-$\beta$ hybrid plasmas, the characteristics of ELM suppression were found consistent with
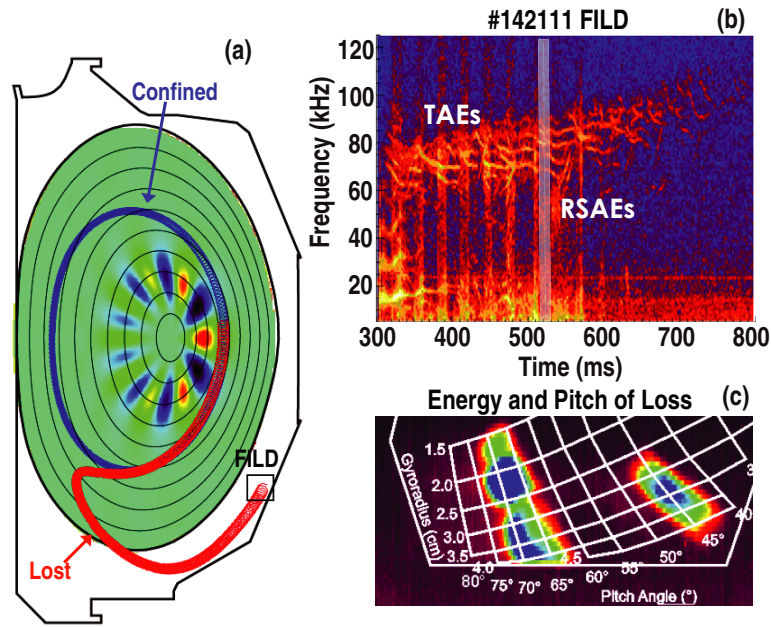
**Figure 11.** (*a*) ORBIT calculations indicate that fast ions lost from the calculated vicinity of TAE and RSAE modes in the core of the plasma can travel to the location of the FILD; (*b*) FILD spectrum includes features that are strongly indicative of TAE and RSAE modes; (*c*) FILD image at 525 ms (time slide indicated by vertical line in (*b*)). Feature on the left-hand side of image is identified as due to prompt loss from NBI, and is unrelated to AE activity. The feature on the right-hand side corresponds to the AEs detected in (*b*), and vanishes later in the discharge when the AE frequency activity has ceased.
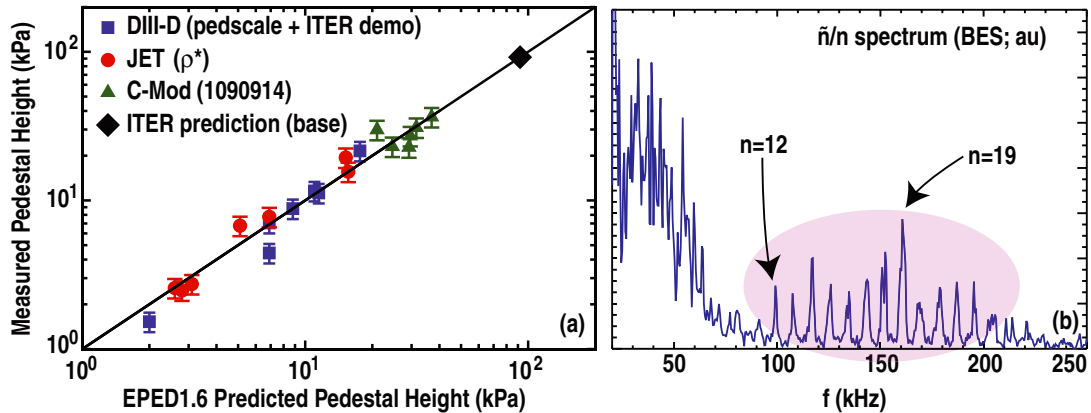


**Figure 12.** (*a*) Initial tests of the EPED1.6 model against data from DIII-D (squares), JET (circles), and C-Mod (triangles) are promising for improved confidence in predicting the pedestal in future experiments, such as ITER (diamond). (*b*) Fluctuations detected by BES measurements in the H-mode pedestal are consistent with expectations for the KBM.
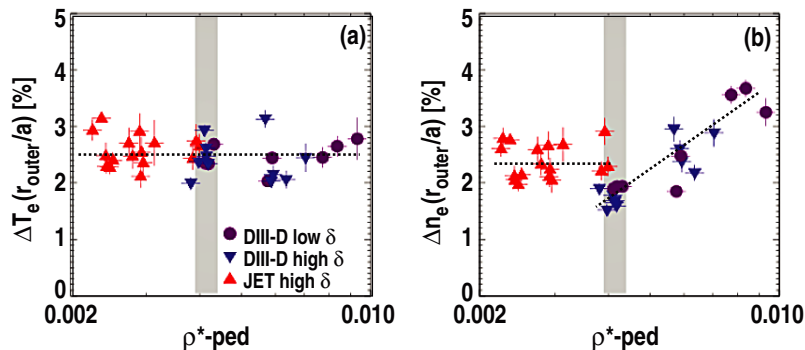


**Figure 13.** Widths of the (*a*) electron temperature and (*b*) electron density pedestal as a fraction of the plasma radius in $\rho^*$ scans performed in JET and DIII-D. The variation of the electron density width in DIII-D is believed to be a consequence of neutral penetration effects.
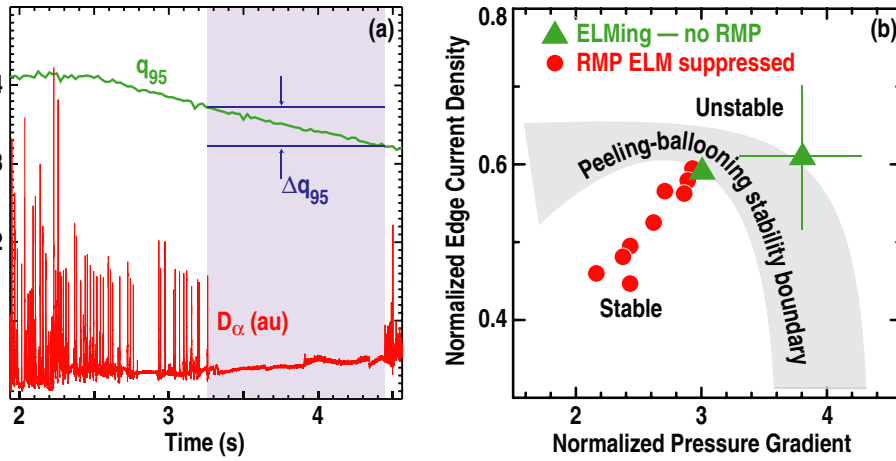
**Figure 14.** (*a*) ELMs are routinely suppressed in DIII-D, over a particular range of safety factors, by $n = 3$ RMP fields driven by currents flowing in internal coils. (*b*) Suppression of ELMs occurs when the pedestal conditions move below the calculated P–B stability boundary.
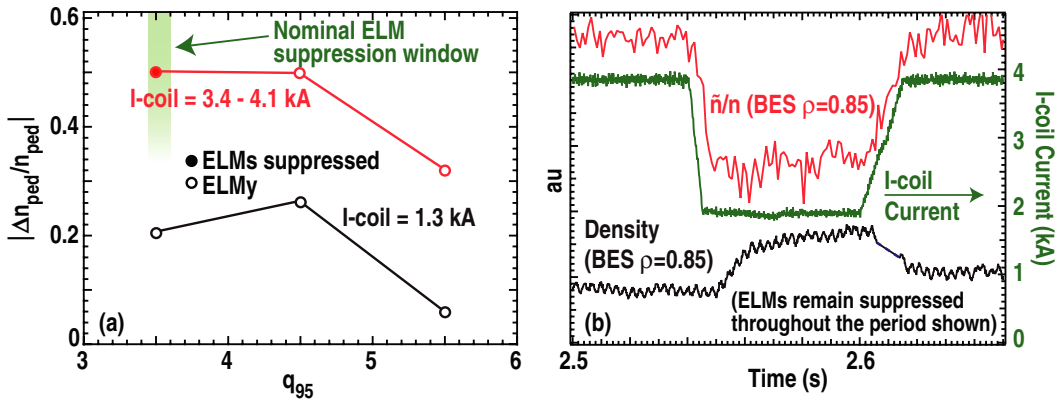


**Figure 15.** (*a*) The pedestal density decreases with increasing current in the RMP coils, but the effect is considerably broader in safety factor than the range where ELMs are suppressed. (*b*) During RMP ELM suppression, reduction in the pedestal density is associated with increased density fluctuations that are in turn correlated with the magnitude of the RMP coil current.
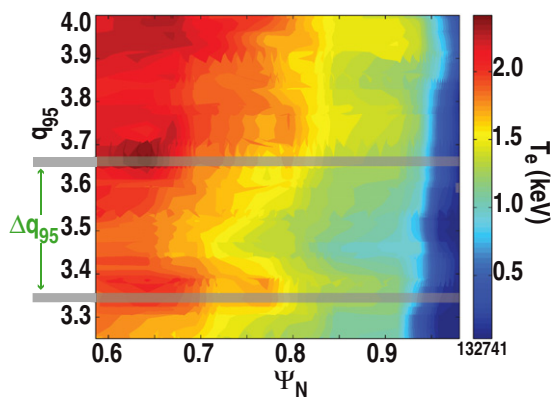


**Figure 16.** The electron temperature gradient is reduced within the ELM suppression window as $q_{95}$ is ramped down.

those in standard H-modes [48]. The shape and magnitude of the edge bootstrap current were observed to affect the confinement of magnetic field lines in the pedestal region, so that a larger bootstrap current separates magnetic resonant surfaces, reduces field line loss from the pedestal top and correlates with a lack of ELM suppression.

Although the impulsive heat load is of the greatest concern, it is desirable to be able to control the steady heat load as well. Recent experiments have been carried out to explore the combination of RMP effects with a radiative divertor, created by injecting gas into the divertor region. In these discharges, ELMs are mitigated, but not fully suppressed, so that at a high pedestal density the peak heat flux is reduced almost to the level of the ELM-suppressed case (figure 17(*a*)). The time-averaged heat flux (figure 17(*b*)) paints a very different picture: the discharges with full RMP ELM suppression exhibit the highest time-averaged heat flux observed, and the radiative divertor discharges are as much as an order of magnitude lower [49].

In recent experiments, DIII-D demonstrated for the first time in the ITER baseline scenario that increased ELM frequency can be achieved via pellet injection [50]. When small pellets are injected from the low-field side of the plasma at 14 Hz, the resulting ELMs occur at an surprisingly fast rate (up to 25 Hz) (figure 18). This can be compared with a natural frequency of about 5 Hz in this scenario. The small pellets do not penetrate the plasma and do not appreciably fuel the core. At the same time as the ELM frequency increases by a factor of about 5, the per-ELM energy loss decreases by a factor of 3–4.
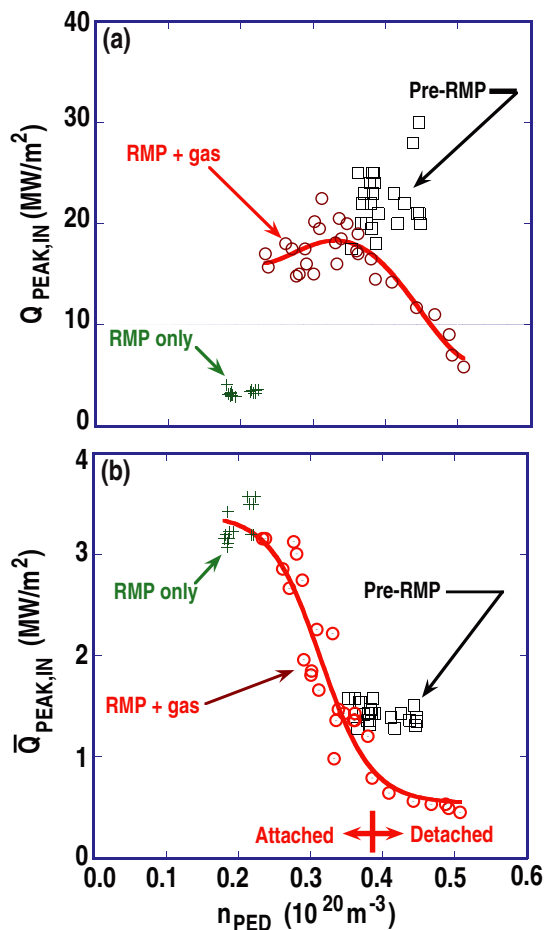
**Figure 17.** (*a*) Peak heat flux is reduced by RMP ELM suppression ('RMP only'). Gas puffing in the divertor ('RMP+gas') increases the peak value, since ELM suppression is lost with addition of the gas. (*b*) The steady, time-averaged, heat flux is the highest with RMP ELM suppression, and is reduced with the addition of gas puffing.



**Figure 18.** ELM pacing via pellet injection has been demonstrated in DIII-D. (*a*) Plasma density is unaffected by pellet injection at a rate of 14 Hz into a plasma with 5 Hz 'natural' ELM frequency. (*b*) The ELM rate increases to approximately 25 Hz, a surprising factor of nearly two faster than the pellet injection. (*c*) $D_\alpha$ emission in a plasma with no pellet injection.

Further experiments are planned using an upgraded injection system, capable of introducing pellets at 30 Hz. ELM pacing has also been observed in phase with a 20 Hz modulation on the I-coil (the same coil as used for the RMP). The ELMs in this case are triggered at both the positive and negative peaks, so the frequency is doubled.

Another approach to eliminating ELMs in tokamaks is to develop operating scenarios that are naturally free of ELMs. QH-mode [35], described in section 3.3.1, is one such scenario, with performance similar to conventional H-mode. The key development needed in QH-mode has been to eliminate the need for strong neutral beam torque, which will not be present in future devices. The present research, using NTV-driven torques to generate the required $E \times B$ shear near the edge, has progressed sufficiently towards that goal so that QH-mode must be considered a possible option for future tokamak operation.

### 4.2. Avoiding and mitigating disruptions

Rapid plasma shutdown via rapid particle delivery is being developed as a last-resort measure to mitigate disruption effects. Th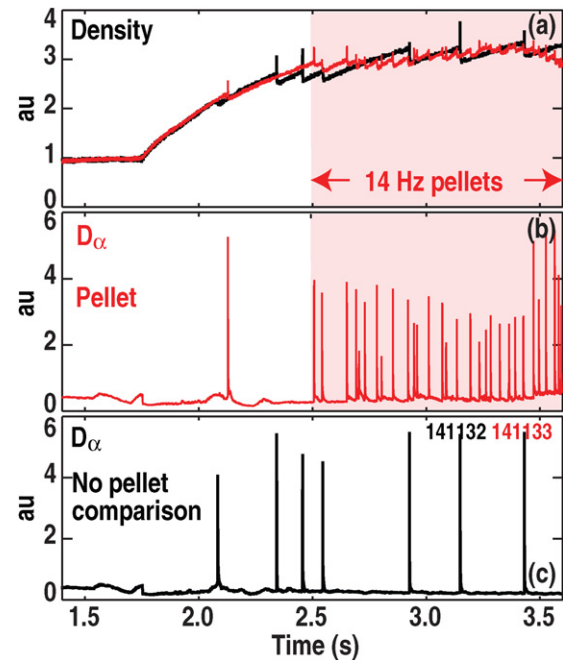is has two roles: first, to rapidly shut down the discharge, and second, to quench the runaway electron (RE) beam that may form. The latter is very challenging due to the theoretically very high densities required. Also, studies with the NIMROD code [51] indicate MHD activity may be less effective in deconfining REs in ITER than in present tokamaks [52].

Previous studies [53] concentrated on massive gas injection (MGI) from valves outside the plasma (figure 19(*a*)). These studies show that particle assimilation is only effective during the thermal quench; particles that arrive later, during the current quench, are ineffective. Recent experiments have explored shattered pellet injection (SPI) as an alternative particle delivery technique (figure 19(*b*)). A large deuterium pellet is injected into the DIII-D vessel, where it strikes a shatter plate, so that the resulting fragments penetrate the plasma [54]. Although more localized than the effect of the MGI, SPI increases the core density to a higher level (as high as $9 \times 10^{21}$ m$^{-3}$, a record density for DIII-D). The deuterium is delivered more rapidly than with MGI in the present valve configuration (figure 19(*c*)), though earlier experiments have shown that the MGI performance can be significantly improved by a higher throughput delivery system [55].

In recent experiments, active control of the current and position of a RE beam has been demonstrated. The beam is produced by injection of an Ar pellet into an inner wall limited plasma (figure 20). With no further intervention, the beam dissipates in less than 50 ms. Initial attempts to control the radial and vertical position of the RE beam have been successful, while the transformer has demonstrated the ability to regulate the current. During the extended RE phase, no direct wall contact, and so no vessel damage, takes place.
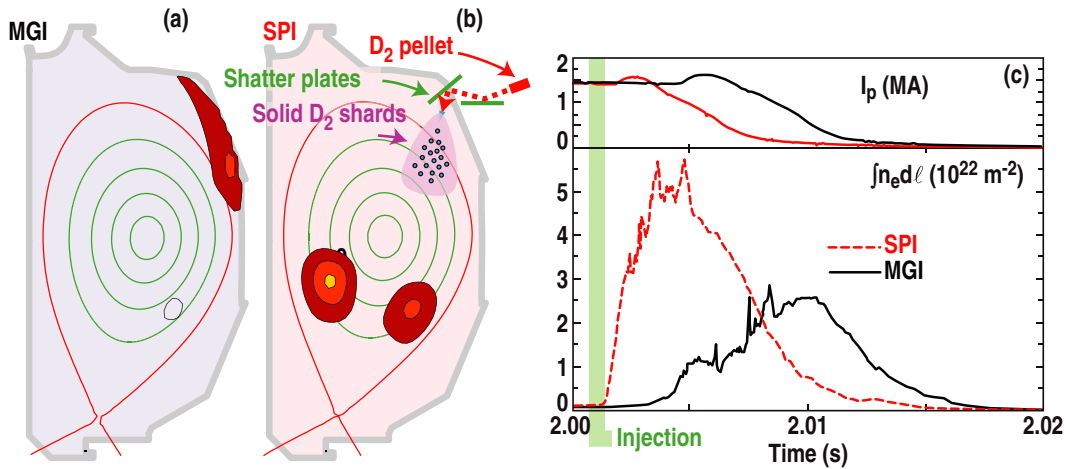
**Figure 19.** (*a*) In MGI, gas is injected from one or more valves, resulting in deposition in the outer part of the plasma. (*b*) SPI deposits particles more centrally. (*c*) The density effect of SPI is both faster and larger (at least locally) than MGI in experiments done to date in DIII-D.
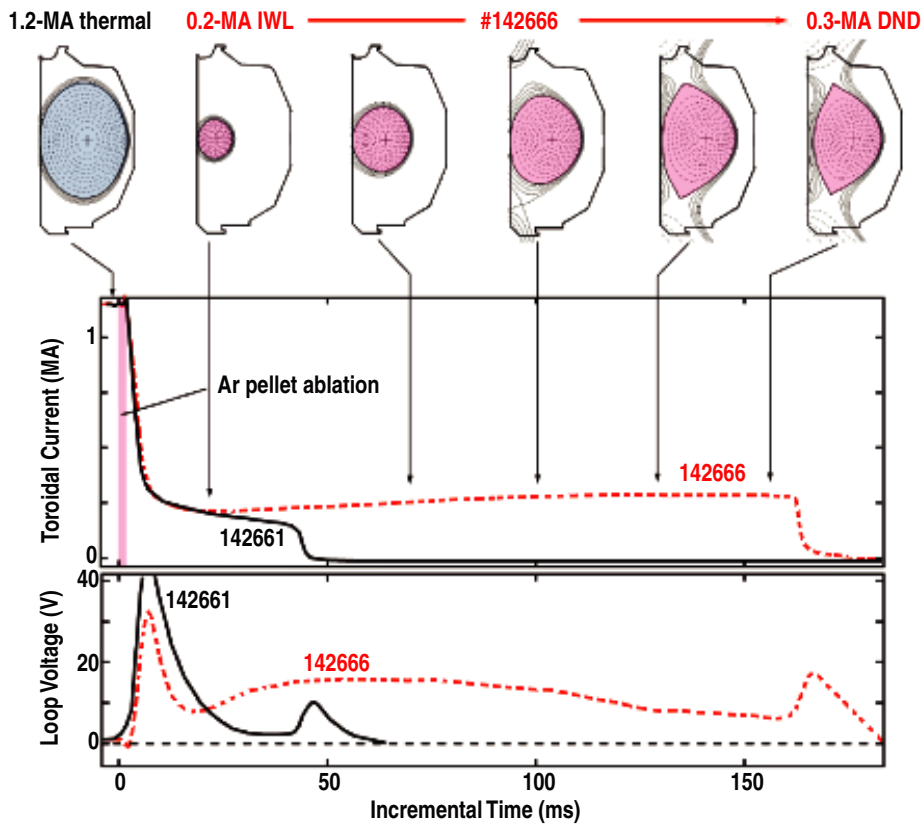


**Figure 20.** A RE channel is produced in inner wall limited discharges in DIII-D by the ablation of an argon pellet. In a discharge with no further intervention, the runaway channel decays rapidly (solid black line). Addition of inductive current drive, in conjunction with active position control, allows sustainment of the RE beam for extended periods of time.

This technique opens the possibility of maintaining the RE beam without risk to hardware, while energy is removed from the beam in a controlled manner, such as simply ramping down the current, or dissipating the energy using the above particle injection techniques. Further experiments are planned to investigate these possibilities. In addition, the RE beam provides a laboratory for measurement of RE growth and decay rates, which are found to be qualitatively consistent with those predicted by RE collisional drag theories.

### 4.3. Tritium retention in plasma facing components

Carbon is an appealing plasma facing material due to its heat tolerance. However, tritium retention is a serious concern for ITER. DIII-D research is working to quantify and develop techniques to mitigate retention.

Dynamic particle balance is used to determine the amount of hydrogenic particles retained in the vessel wall. Here, the sources (gas injection and, where applicable, neutral
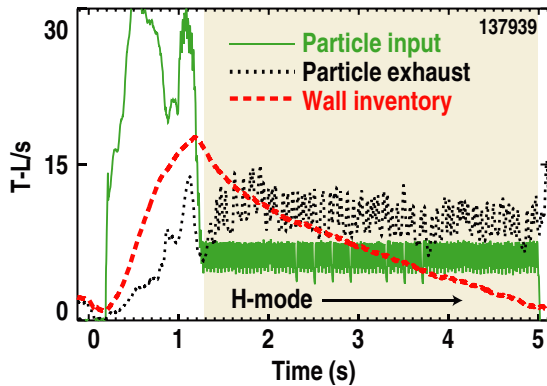
**Figure 21.** Time history of particle input and exhaust, and the wall inventory calculated by dynamic particle balance. The wall absorbs a large fraction of the gas introduced during the ohmic and L-mode phases, but the entire inventory is removed during an extended ELMing H-mode phase.



**Figure 22.** Approximately half of the deuterium inventory was removed from DIII-D during a 2 h, 350 °C, bake with a 2 Torr partial pressure of $O_2$ (star), consistent with laboratory tests (circles) carried out at the University of Toronto under similar conditions. Further tests at the University of Toronto (triangles) indicate that virtually all of the deuterium can be removed by baking at a higher $O_2$ partial pressure.

beams) and exhaust (cryopumps) are monitored, with the remaining particles assumed deposited in plasma facing surfaces. This technique has been used in both DIII-D and Alcator C-Mod, and has been successfully benchmarked against static measurements of vessel pressure before and after a discharge. Figure 21 shows an example of dynamic particle balance during an H-mode discharge in DIII-D. Although there is finite loading during the ohmic and L-mode phases, surprisingly, the wall absorbs no additional particles during the H-mode. This result does not depend on the heating source; in both ECH- and NBI-heated H-mode discharges, the vessel inventory returns to its pre-shot level at the end of the discharge.

This does not preclude hydrogen from being bound up with eroded carbon that redeposits at less exposed locations. DIII-D has tested thermal oxidation as a technique for removing these co-deposits. Prior to the experiment, an extensive laboratory testing programme was carried out at the University of Toronto. The DIII-D vessel was then filled with a 10 Torr He : $O_2$ = 90 : 10 mixture (∼1 Torr $O_2$ partial pressure) and baked for 2 h at 350 °C, with pre-characterized sample tiles inserted. Estimates made by monitoring gas removed during and after the bake indicate about half of the co-deposits were removed (figure 22). This result is consistent with expectations based on lab tests at the same partial pressure of $O_2$. Further lab tests indicate that a larger fraction of the deposits can be removed from the tiles by increasing the pressure. Following the bake, high-performance hybrid plasmas were obtained after a short clean-up period. $O_2$ baking did not damage internal components, and did not compromise the vessel conditions needed for advanced scenarios [56].

## 5. Specific ITER research plan issues

As ITER approaches its construction phase, DIII-D is increasing its emphasis on predictive understanding of physics governing ITER's behaviour. However, DIII-D continues to respond to specific ITER concerns, now increasingly focused on development of the research plan. We report on two such areas of focused DIII-D research here.
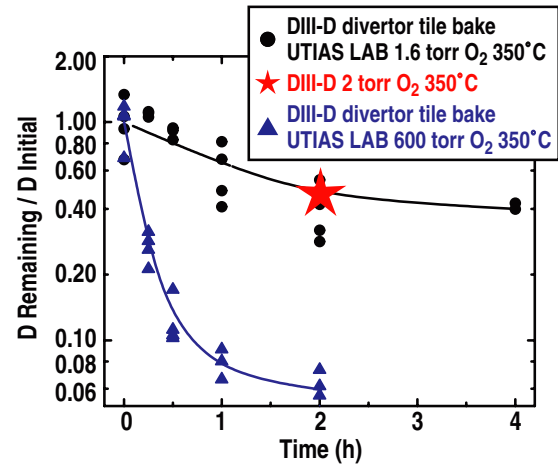
### 5.1. Characterization of the L–H threshold

A set of experiments was performed to determine H-mode access requirements for ITER's first (non-nuclear H and He) and second (activated D) operational phases. These experiments [57] build on previous work [58] demonstrating that the L–H transition threshold power $P_{TH}$ increases with positive (parallel to $I_P$) rotation in both H and D plasmas. Similar behaviour was confirmed in He plasmas. $P_{TH}$ for the three species occurs approximately at the following ratios: $P_{TH}$ (D : He : H) ≈ (1 : 1.4 ± 0.1 : 2.1 ± 0.1). An intermediate case, with H-NBI injected into He plasmas, exhibits thresholds between pure H and He, depending on the species' relative concentrations.

The density dependence of the H-mode power threshold is a key component of the ITPA2008 scaling [59]. Many devices, including DIII-D, observe a minimum in density that contrasts with this scaling. This minimum is seen in the new results (figure 23), in both D and He plasmas, albeit at different densities. Also, as previously observed, $P_{TH}$ in He is higher than in D at low densities, with the two cases moving closer together with increasing density.

Another finding of this study is the steady decrease in $P_{TH}$ as the X-point moves closer to the divertor. This, combined with choosing the 'right' density, may provide a path to obtain H-mode during the non-nuclear phase of ITER. These experiments also showed applying resonant magnetic fields with the RMP ELM control coils can increase the power threshold.

### 5.2. Predict the impact of TBM on ITER's performance

ITER will include three pairs of toroidally localized TBMs whose ferromagnetic structural materials will perturb the magnetic field. Theory to predict the impact of these field perturbations on performance is lacking, so DIII-D simulated the effect with a mockup (figure 24(*a*)) of a single TBM set
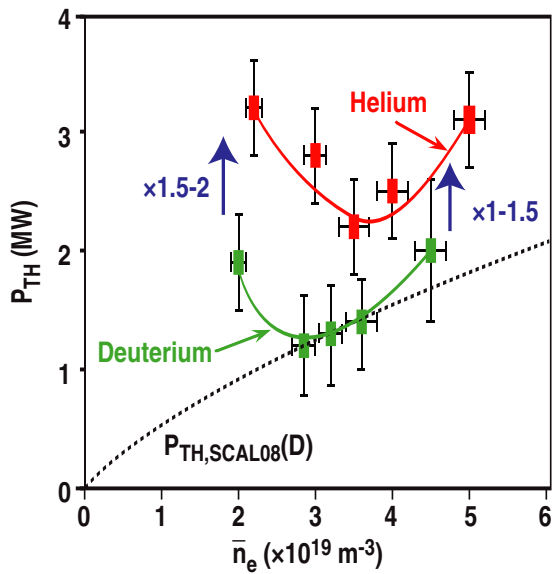
**Figure 23.** The H-mode power threshold as a function of the line-integrated L-mode density for D and He plasmas (1.0 MA, 1.65 T) with auxiliary heating by ECH. The dotted line corresponds to the ITPA2008 power threshold scaling relation for D plasmas. The results with balanced (torque free) NBI are very similar.

with coils driving fields up to $\sim$3$\times$ the relative amplitude of those in ITER. The TBM mockup assembly was inserted into a midplane port on DIII-D for these experiments. It was subsequently removed, but can be reinserted for future experiments.

Measurements were made of the TBM's impact on parameters including L–H threshold, confinement, rotation and EPs [60]. The effect on rotation and confinement quality is shown in figure 24(*b*). Here, the local ripple $\delta \equiv (B_{max} - B_{min})/(B_{max} + B_{min})$ is the combined ripple arising from both the TBM and toroidal field coil non-axisymmetries. The equivalent value for ITER, in front of a TBM, is $\delta \approx 1.2\%$, and the DIII-D coil at full current (1.2 kA) is capable of reaching approximately 3.6%. In these experiments, we found only small effects on performance with the TBM mockup current set to match the ITER value. Decreased confinement and toroidal rotation were observed, but only when the coil current was increased to produce 2–3 times the ripple anticipated in ITER. Global losses of fast ions were small [61].

These experiments were carried out at $\beta_N \approx 2.2$, somewhat higher than $\beta_N \approx 1.8$ anticipated in the ITER baseline scenario. We chose the higher pressure because the effect on stored energy and density increases strongly with $\beta_N$, the results were much clearer at the higher $\beta$.

Even where detrimental effects are seen, it may be possible to minimize them by reoptimizing the magnetic error field correction in DIII-D, a technique that is directly applicable to ITER. Calculations with IPEC [62] indicate that amplification of the $n = 1$ perturbation is responsible for the majority of the NTV torque on the plasma, which in turn, we speculate, is responsible for the negative impact on rotation (figure 25(*a*)). Further calculations indicate that the $n = 1$ component can be attenuated using error field correction techniques. Initial experiments in DIII-D appear to confirm this. As shown in figure 25(*b*), the density at the onset of locked modes, an

indicator of the tokamak plasma's sensitivity to error fields, increases with increasing TBM coil current. Reoptimization of the error field correction reduces the threshold to its previous level prior to introduction of the TBM field. These experiments were carried out in low-pressure L-mode plasmas; further experiments are planned to demonstrate the applicability of this technique to H-mode.

## 6. Summary and future research directions

We have described recent DIII-D research highlights in several areas; the references herein provide the reader a more complete discussion of these results.

Recent efforts to optimize steady-state scenarios focus on the relationship between transport and the current profile. This relationship is not captured by present transport models, so the data obtained from these studies can in turn drive further developments of those models. Aspects of other scenarios have been studied, including $\rho^*$ scaling of advanced inductive scenarios and generation of QH-mode without an external torque. Safe access to and exit from ITER operating scenarios have been studied, with full discharge scenarios demonstrated in several different regimes. Future work will benefit from fast wave heating and additional ECH/CD both for tailoring profiles and establishing more reactor-relevant conditions by primarily heating electrons. Off-axis NBI will provide additional control of the current profile.

Validation of physics-based models is a major emphasis across the DIII-D programme. Here we described such efforts in transport, rotation, energetic particles and the H-mode pedestal. These are given as examples; the approach of using modelling to design and interpret experiments permeates the DIII-D programme. Future opportunities will take advantage of additional diagnostics, already commissioned and currently undergoing construction or upgrade.

Methods to control steady and transient particle and energy fluxes are extremely important to ensure the reliable operation and survivability of future devices. DIII-D has pioneered the use of resonant magnetic perturbations to suppress ELMs and remove their damaging effects. Recent research points to the relationship between the applied magnetic perturbation and thermal transport as the key. Further experiments and theory are being prepared to focus on the detailed effects of imposed three-dimensional magnetic fields on the plasma, especially the mechanisms under which transport is increased. We are also developing alternative strategies, including pellet ELM pacing. Another approach under study is to identify naturally ELM-free operational scenarios. An example is the QH-mode, which has for the first time been maintained without an external torque driven by neutral beams.

DIII-D has also explored techniques to mitigate the damaging effects of disruptions by introducing large quantities of particles to the plasma. A major challenge of this line of research has been to introduce a sufficient number of particles to prevent the development of a RE beam. Recently, DIII-D has demonstrated position control of this beam, opening the possibility of allowing it to safely dissipate in a controlled manner.

Experiments continue to evaluate carbon as a first wall material in tokamaks. We have determined that deuterium is
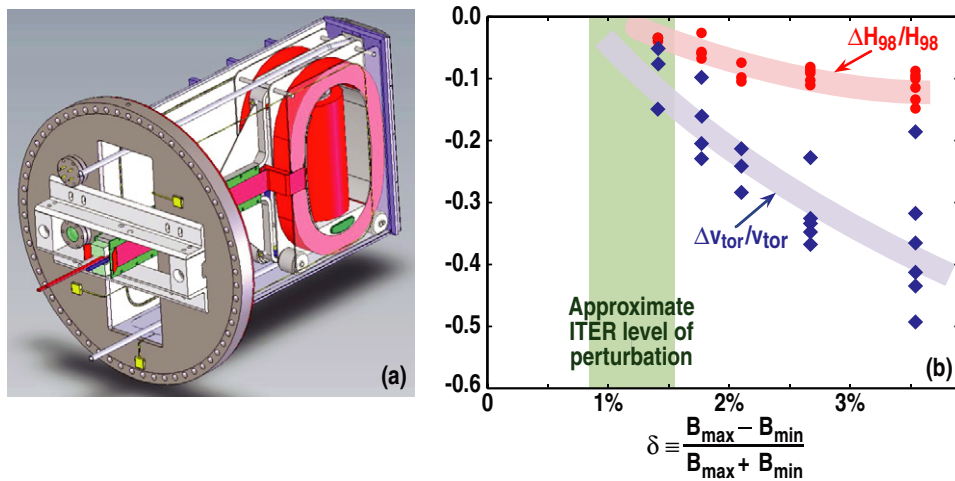
**Figure 24.** (*a*) The TBM mockup, combining toroidal racetrack coils and a poloidal solenoid, was inserted in a radial port on DIII-D. Currents in the two sets of coils simulate the field perturbation in ITER arising from a single set of TBMs. (*b*) Relative reductions of confinement factor $H_{98}$ and toroidal velocity as a function of the local ripple $\delta$ at $\beta_N \approx 2.2$. Below the ITER perturbation level, the effect on confinement was too small to measure.
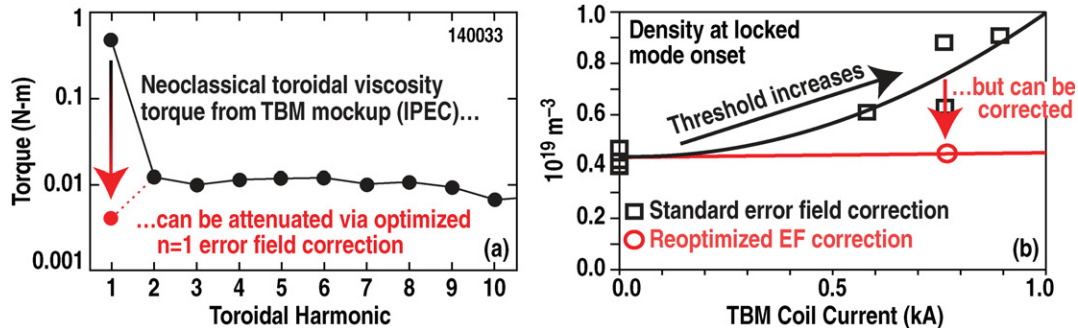


**Figure 25.** (*a*) Calculations with IPEC indicate that the NTV torque imposed by the TBM mockup on the plasma is primarily due to amplification of the $n = 1$ field component (black circles). Optimization of the $n = 1$ field error correction is expected to attenuate this effect. (*b*) Susceptibility of the plasma to low-density locked modes is used to gauge the effect of error fields. The effect increases with current in the TBM, but is cancelled via reoptimization of the error field correction as predicted by IPEC.

actually removed from the wall during H-mode. Hydrogen-bearing co-deposits that are shadowed from the plasma can be removed by baking the vessel in an atmosphere containing oxygen.

The DIII-D research programme has demonstrated strong interest and ability to respond to ITER's short- and long-term needs. Experiments with D, H and He plasmas are contributing to plans for the initial operation of ITER, while at the same time producing a large dataset useful for confinement and transport research.

Finally, DIII-D responded to an ITER-identified need for tests of the effects of the TBM on plasma performance, with the favourable result that at ITER equivalent perturbation strength and beta, little or no degradation is seen in performance. Further experiments are being planned to verify that even the small effects seen in ITER-like conditions can be attenuated by reoptimizing the error field control.

DIII-D is currently planning experiments to be carried out during the next campaign, and further into the future. These activities will take advantage of improvements that are currently underway, including additional EC power, flexible aiming of NBI, and a large number of new and improved diagnostics. We anticipate continued production of

exciting results in support of ITER and other devices on the development path to fusion as an attractive power source.

## Acknowledgment

## Appendix. The DIII-D Team

G. Abla[1], M.M. Abrahim[1], E.O. Allen[1], S.L. Allen[2], D.D. Anastasi[1], P.M. Anderson[1], M.E. Austin[6], F.W. Baity[4], J.P. Bakalarski[1], C.P. Balance[5], I. Balboa[6], E.M. Bass[7], D.J. Battaglia[4], C.B. Baxi[1], L.R. Baylor[4], M. Becoulet[8], E.A. Belli[7], J.W. Berkery[9], L.A. Berry[4], M.N.A. Beurskens[6], J.M. Bialek[9], J.A. Boedo[10], I.N. Bogatu[11], R.L. Boivin[1], P. Bonoli[12], A.H. Boozer[9], B.D. Bray[1], D.P. Brennan[5], S. Brezinsek[14], N.H. Brooks[1], D. Buchenauer[15], R.V. Budny[16], R. Bulmer[2], P. Burratti[11], K.H. Burrell[1], R.J. Buttery[1], J.D. Callen[18], R.W. Callis[1], G.L. Campbell[1], J.M. Candy[1], J.M. Canik[4], T.N. Carlstrom[1], T.A. Carter[19], W.P. Cary[1], T.A. Casper[2], M. Cengher[1], C.D. Challis[6], F.R. Chamberlain[1],

V.S. Chan[1], M.S. Chance[16], C.S. Chang[20], J.A. Chavez[1], B. Chen[1], R. Chipman[21], H.K. Chiu[1], M. Choi[1], C. Chrobak[1], C. Chrystal[10], M.S. Chu[1], V. Chuyanov[22], I.G.J. Classen[23], A.J. Cole[18], N. Commaux[4], F. Crisanti[17], N.A. Crocker[19], G. Cunningham[6], D.S. Darrow[16], J.W. Davis[24], E. de la Luna[25], P. de Vries[23], J.C. DeBoo[1], J.S. deGrassie[1], S.J. DePasquale[16], T.M. Deterly[1], P.H. Diamond[10], J.L. Doane[1], C.W. Domier[26], J. Dorris[12], E.J. Doyle[19], K. Dubovenko[1], J. Edwards[16], T. Eich[27], N.W. Eidietis[1], J.D. Elder[24], R. Ellis[2], R.A. Ellis[16], R.F. Ellis[28], A.L. Equizabal[16], T.E. Evans[1], M.E. Fenstermacher[2], J.R. Ferron[1], D.K. Finkenthal[29], R.K. Fisher[1], B.W.N. Fitzpatrick[24], S.M. Flanagan[1], J. Flanagan[6], R.J. Fonck[18], L. Frassinetti[30], E. Fredd[16], E.D. Fredrickson[16], H.G. Frerichs[14], C. Fuchs[27], S. Gao[31], X. Gao[31], M. García-Muñoz[27], A.M. Garofalo[1], D.A. Gates[16], R. Geer[2], K.W. Gentle[3], A. Geraud[8], S. Gerhardt[16], E. Giovannozzi[32], C. Giroud[6], P. Gohil[1], N.N. Gorelenkov[16], Y.A. Gorelov[1], R.H. Goulding[4], R.S. Granetz[12], D.L. Green[4], K.L. Greene[1], C.M. Greenfield[1], N.L. Greenough[16], Y. Gribov[22], B.A. Grierson[16], R.J. Groebner[1], W.H. Grosnickle[1], M. Groth[2, 47], H.J. Grunloh[1], W. Guo[31], T.J. Guzman[1], A.A. Haasz[24], T.S. Hahm[16], S.H. Hahn[33], J. Hansink[1], G.R. Hanson[4], J.M. Hanson[9], R.W. Harvey[34], A. Hassanein[35], C.C. Hegna[18], W.W. Heidbrink[36], A. Herrmann[27], D.N. Hill[2], J.C. Hillesheim[19], D.L. Hillis[4], J.K. Hobirk[27], C.T. Holcomb[2], C. Holland[10], E.M. Hollmann[10], K.L. Holtrop[1], R.M. Hong[1], A.R. Horton[4], L.D. Horton[27], J.C. Hosea[16], J. Howard[37], D.M. Hoyt[1], C.L. Hsieh[1], A. Huber[14], B. Hudson[7], J.W. Hughes[12], D.A. Humphreys[1], P. Huynh[1], G.T.A. Huysmans[8], A.W. Hyatt[1], S. Ide[38], F. Imbeaux[8], Y. In[11], R.C. Isler[4], V.A. Izzo[10], S. Jachmich[39], G.L. Jackson[1], W. Jacob[27], E.F. Jaeger[4], M.W. Jakubowski[40], A.N. James[10], R.J. Jayakumar[1], I. Jenkins[6], Y.M. Jeon[41], T.C. Jernigan[4], H. Jhang[33], E.H. Joffrin[8], R.D. Johnson[1], P. Johnson[42], I. Joseph[2], A. Kallenbach[27], R.C. Kalling[1], D.H. Kaplan[1], O. Katsuro-Hopkins[9], S.M. Kaye[16], K.M. Keith[1], A.G. Kellman[1], D.H. Kellman[1], M. Kempenaars[6], C.E. Kessel[16], E.N. Kim[1], L. Kim[1], J.S. Kim[11], S.H. Kim[43], J.D. King[44], J.E. Kinsey[1], A. Kirk[6], A. Kirschner[14], F. Kochl[45], N. Kohen[46], C. Konz[40], T. Koskela[47], G.J. Kramer[16], S.I. Krasheninnikov[10], K. Krieger[27], J.A. Kulchar[1], T. Kurki-Suonio[47], R.J. La Haye[1], B. LaBombard[12], R. Laengner[14], M.J. Lanctot[2], L.L. Lao[1], C.J. Lasnier[2], E.A. Lazarus[4], R.L. Lee[1], X. Lee[1], A.W. Leonard[1], J.A. Leuer[1], G.Q. Li[31], Z. Lin[36], A. Litnovsky[14], C. Liu[1], Y.Q. Liu[6], D. Liu[18], S. Liu[31], A. Loarte[22], S.D. Loch[5], L.L. Lodestro[2], N. Logan[48], J. Lohr[1], P. Lomas[6], J. Lonnroth[47], T.C. Luce[1], N.C. Luhmann Jr[26], G. Maddison[6], C.F. Maggi[27], M.A. Mahdavi[49], R. Maingi[4], M.A. Makowski[2], M. Marot[50], L. Marrelli[32], P. Martin[32], D. Mastrovito[16], G. Matsunaga[38], P.S. Mauzey[1], D.C. McCune[16], W.L. McDaniel[1], D.C. McDonald[6], B.B. McHarg[1], G.R. McKee[18], A.G. McLean[4], J.E. Menard[16], W.H. Meyer[2], O. Meyer[51], D. Mikkelsen[16], D.C. Miller[1], C.P. Moeller[1], S. Mordijck[10], K. Morris[2], E.C. Morse[44], R.A. Moyer[10], Y.R. Mu[24], D. Mueller[16], S.H. Müller[10], H.W. Müller[27], J.M Muñoz Burgos[7], M. Murakami[4], C.J. Murphy[1], C.M. Muscatello[36], A. Nagy[16], E. Nardon[8], M.F.F. Nave[52], G.A. Navratil[9], R. Nazikian[16], H. Nehme[8], J. Neilson[53],

S. Noraky[1], I. Nunes[54], R.E. Nygren[15], R.C. O'Neill[1], Y.K. Oh[33], M. Okabayashi[16], R.A. Olstad[1], G.M. Olynyk[12], D.M. Orlov[10], T.H. Osborne[1], Y. Ou[41], L.W. Owen[4], N. Oyama[38], N.A. Pablant[10], D.C. Pace[36], C. Pan[31], A.Y. Pankin[41], J.M. Park[4], J.K. Park[16], G. Park[20], H.K. Park[55], C.T. Parker[1], P.B. Parks[1], R. Pasqualotto[17], C.J. Pawley[1], L.D. Pearlstein[2], W.A. Peebles[19], B. Pegourie[8], B.G. Penaflor[1], P.I. Petersen[1], T.W. Petrie[1], C.C. Petty[1], N.Q. Pham[1], V. Philipps[14], D.A. Piglowski[1], R.I. Pinsker[1], P. Piovesan[32], L. Piron[32], R.A. Pitts[22], P.A. Politzer[1], D.M. Ponce[1], M. Porkolab[12], G.D. Porter[2], A. Pospieszczyk[14], R. Prater[1], V.D. Pustovitov[56], J.P. Qian[31], N. Ramasubramanian[57], D.A. Rasmussen[4], H. Reimerdes[9, 58], D. Reiter[14], Q.L. Ren[31], M.E. Rensink[2], T.L. Rhodes[19], H. Rinderkhecht[16], T.D. Rognlien[2], G. Rossi[16], J.C. Rost[12], D.L. Rudakov[10], P.M. Ryan[4], D. Ryutov[2], S. Saarelma[6], S.A. Sabbagh[9], G. Saibene[59], A. Salmi[47], U. Samm[14], B.S. Sammuli[1], R. Sartori[59], O. Sauter[58], R.I. Savercool[1], M.J. Schaffer[1], D.P. Schissel[1], D.J. Schlossberg[18], O. Schmitz[14], L. Schmitz[19], E. Schuster[41], E. Scime[60], J.T. Scoville[1], M.W. Shafer[18], M. Shapiro[12], J.P. Sharpe[61], K. Shinohara[38], K.C. Shoolbred[1], P.E. Sieck[1], A.C.C. Sips[27], R.D. Smirnov[10], J.P. Smith[1], S. Smith[1], J.A. Snipes[22], P.B. Snyder[1], E.R. Solano[25], W.M. Solomon[16], A.C. Sontag[4], A. Soppelsa[32], K.H. Spatschek[62], D.A. Spong[4], R. Srinivasan[57], H.E. St John[1], W.M. Stacey[63], G.M. Staebler[1], R.D. Stambaugh[1], P.C. Stangeby[24], R. Stemprok[1], T. Stevenson[16], H. Stoschus[14], E.J. Strait[1], R.W. Street[1], W. Suttrop[27], T. Suzuki[27], V. Svidzinski[11], T. Tala[64], D.A. Taussig[1], P.L. Taylor[1], T.S. Taylor[1], D.M. Thomas[1], B.J. Tobias[26], J.F. Tooker[1], C.K. Tsui[24], F. Turco[7], A.D. Turnbull[1], G.R. Tynan[10], M. Umansky[2], K.R. Umstadter[10], E.A. Unterberg[4], I.U. Uzun-Kaymak[18], M.A. Van Zeeland[1], S. Visser[1], F. Volpe[18], A. von Halle[16], M.R. Wade[1], M.L. Walker[1], M. Walsh[6], R.E. Waltz[1], W.R. Wampler[15], B.N. Wan[31], G. Wang[19], H.Z. Wang[31], J.G. Watkins[15], A.S. Welander[1], J.C. Wesley[1], W.P. West[1], A.E. White[12], R.B. White[16], D.G. Whyte[12], S. Wiesen[14], J.R. Wilson[16], H.R. Wilson[65], A. Wingen[62], M. Wischmeier[27], R.C. Wolf[40], E. Wolfrum[27], C.P.C. Wong[1], S.K. Wong[66], W. Wu[1], S.J. Wukitch[12], B.J. Xiao[31], X. Xu[2], Z. Yan[18], H.H. Yip[1], S.-W. Yoon[33], K.-I. You[33], D. Young[67], J.H. Yu[10], Q.P. Yuan[31], L. Zabeo[6], D. Zarzoso[68], L. Zeng[19], W. Zhang[19] and Y.B. Zhu[36]

## Affiliations

[1] General Atomics, USA
[2] Lawrence Livermore National Laboratory, USA
[3] University of Texas, USA
[4] Oak Ridge National Laboratory, USA
[5] Auburn University, USA
[6] EURATOM/CCFE Fusion Association, Culham Science Centre, UK
[7] Oak Ridge Institute of Science Education, USA
[8] Association Euratom CEA, DSM/IRFM, Cadarache, France
[9] University of California, San Diego, USA
[10] Columbia University, USA
[11] FAR-TECH, Inc., USA
[12] Massachusetts Institute of Technology, USA
[13] University of Tulsa, USA

[14] EURATOM-FZ Jülich, Germany
[15] Sandia National Laboratories, USA
[16] Princeton Plasma Physics Laboratory, USA
[17] ENEA-Frascati, Italy
[18] University of Wisconsin, USA
[19] University of California, Los Angeles, USA
[20] Courant Institute, New York University, USA
[21] University of Arizona, USA
[22] ITER Organization, Cadarache, France
[23] Association EURATOM-FOM Rijnhuizen, The Netherlands
[24] University of Toronto, Canada
[25] Association EURATOM-CIEMAT, Madrid, Spain
[26] University of California, Davis, USA
[27] Max Plank Institut für Plasmaphysik, Garching, Germany
[28] University of Maryland, USA
[29] Palomar College, USA
[30] Association EURATOM-VR, Alfven Laboratory, Stockholm, Sweden
[31] ASIPP-Hefei, People's Republic of China
[32] Consorzio RFX, Italy
[33] National Fusion Research Institute, Korea
[34] CompX, USA
[35] Purdue University, USA
[36] University of California, Irvine, USA
[37] Australian National University, Australia
[38] Japan Atomic Energy Agency (JAEA), Japan
[39] Association EURATOM, Belgium
[40] Max Plank Institut für Plasmaphysik, Greifswald, Germany
[41] LeHigh University, USA
[42] Butler University, USA
[43] Korea Atomic Energy Research Institute, Korea
[44] University of California, Berkeley, USA
[45] Association EURATOM-OAW/ATI, Vienna, Austria
[46] University of Marseille, France
[47] Helsinki University of Technology, Finland
[48] Brown University, USA
[49] ALITRON
[50] University of Basel, Switzerland
[51] Association Euratom CEA, DSM/IRFM, Cadarache, France
[52] EURATOM Lisbon
[53] Lexam Research, Redwood City, USA
[54] Association EURATOM-IST, Lisbon
[55] Pohang University of Science & Technology, Korea
[56] Institute for Tokamak Physics, Moscow, Russia
[57] Institute for Plasma Research, India
[58] CRPP-EPFL-Lausanne, France
[59] Fusion for Energy Joint Undertaking, Barcelona, Spain
[60] West Virginia University, USA
[61] Idaho National Laboratory, USA
[62] Heinrich-Heine University, Düsseldorf, Germany
[63] Georgia Institute of Technology, USA
[64] Association EURATOM-Tekes, Finland
[65] University of York, UK
[66] Mesa College, USA
[67] National Renewable Energy Laboratory, USA
[68] Ecole Polytechnique, France

## References

[1] Petty C.C. *et al* 2003 *Nucl. Fusion* **43** 700
[2] Park J.-M. *et al* 2009 *Phys. Plasmas* **16** 092508
[3] Bickerton R.J. *et al* 1971 *Nature Phys. Sci.* **229** 110
[4] Ferron J.R. *et al* 2010 Optimization of the safety factor profile for high noninductive current fraction discharges in DIII-D *Nucl. Fusion* submitted
[5] Holcomb C.T. *et al* 2010 Dependence of transport on the safety factor profile in DIII-D steady-state scenarios *Proc. 37th EPS Conf. on Plasma Physics (Dublin, Ireland, 21–25 June 2010)* paper P1.1108 http://ocs.ciemat.es/EPS2010PAP/pdf/P1.1108.pdf
[6] Staebler G.M., Kinsey J.E. and Waltz R.E. 2007 *Phys. Plasmas* **14** 055909
[7] Holcomb C.T. *et al* 2011 The effect of safety factor profile on transport in steady-state, high-performance scenarios *Phys. Plasmas* in preparation
[8] Greenfield C.M. *et al* 2004 *Phys. Plasmas* **11** 2616
[9] Reimerdes H. *et al* 2010 Evidence for the importance of trapped particle resonances for resistive wall mode stability in high beta tokamak plasmas *Phys. Rev. Lett.* submitted
[10] Okabayashi M. *et al* 2010 Off-axis fishbone-like instability and excitation of the resistive wall mode (RWM) in JT-60U and DIII-D devices *Phys. Plasmas* submitted
[11] In Y. *et al* 2011 Error field correction in unstable resistive wall mode (RWM) regime *Nucl. Fusion* submitted
[12] Luce T.C. *et al* 2010 Development of advanced inductive scenarios for ITER *Proc. 23rd IAEA Conf. on Fusion Energy (Daejeon, Republic of Korea, 11–16 October 2010)* paper ITR/1-5 http://www-pub.iaea.org/MTCD/Meetings/PDFplus/2010/cn180/cn180_papers/itr_1-5.pdf
[13] Romanelli F. *et al* 2011 Overview of JET results *Nucl. Fusion* submitted
[14] Politzer P.A. *et al* 2010 Understanding confinement in advanced inductive scenario plasmas—dependence on gyroradius and rotation *Proc. 23rd IAEA Conf. on Fusion Energy (Daejeon, Republic of Korea, 11–16 October 2010)* paper EXC/P2-06 http://www-pub.iaea.org/MTCD/Meetings/PDFplus/2010/cn180/cn180_papers/exc_p2-06.pdf
[15] Crotinger J.A. *et al* 1997 *LLNL Report* UCRL-ID-126284, available from NTIS #PB2005-102154
[16] Casper T.A. *et al* 2011 *Nucl. Fusion* **51** 013001
[17] Jackson G.L. *et al* 2010 DIII-D experimental simulation of ITER scenario access and termination *Proc. 23rd IAEA Conf. on Fusion Energy (Daejeon, Republic of Korea, 11–16 October 2010)* paper EXS/P2-11 http://www-pub.iaea.org/MTCD/Meetings/PDFplus/2010/cn180/cn180_papers/exs_p2-11.pdf
[18] Park J.M. *et al* 2010 Experiment and modeling of ITER demonstration discharges in the DIII-D tokamak *Proc. 23rd IAEA Conf. on Fusion Energy (Daejeon, Republic of Korea, 11–16 October 2010)* paper EXC/P2-05 http://www-pub.iaea.org/MTCD/Meetings/PDFplus/2010/cn180/cn180_papers/exc_p2-05.pdf
[19] Rhodes T.L. *et al* 2011 Multi-scale/multi-field turbulence measurements to rigorously test gyrokinetic simulation predictions on the DIII-D tokamak *Nucl. Fusion* at press
[20] Holland C. *et al* 2010 Advances in validating gyrokinetic turbulence models in L and H mode plasmas *Phys. Plasmas* at press
[21] DeBoo J.C. *et al* 2010 *Phys. Plasmas* **17** 056105
[22] Schmitz L. *et al* 2010 Reduced electron thermal transport in low collisionality H-mode plasmas in DIII-D and the importance of small-scale turbulence *Proc. 23rd IAEA Conf. on Fusion Energy (Daejeon, Republic of Korea, 11–16 October 2010)* paper EXC/P7-01 http://www-pub.iaea.org/MTCD/Meetings/PDFplus/2010/cn180/cn180_papers/exc_p7-01.pdf
[23] Candy J. and Waltz R.E. 2003 *Phys. Rev. Lett.* **91** 045001

[24] deGrassie J.S. *et al* 2009 *Plasma Phys. Control. Fusion* **51** 124047
[25] Solomon W.M. *et al* 2009 *Nucl. Fusion* **49** 085005
[26] Gurcan O.D. *et al* 2007 *Phys. Plasmas* **14** 042306
[27] Solomon W.M. *et al* 2011 Characterization of the effective torque profile associated with driving intrinsic rotation on DIII-D *Nucl. Fusion* submitted
[28] Müller S.H. *et al* 2011 Intrinsic rotation from an edge co-current rotation layer and evidence for kinetic momentum transport mechanisms in DIII-D H-mode plasmas *Phys. Rev. Lett.* submitted
[29] deGrassie J.S. *et al* 2009 *Nucl. Fusion* **49** 085020
[30] Cole A.J. *et al* 2011 Observation of peak neoclassical toroidal viscous force in the DIII-D tokamak *Phys. Rev. Lett.* submitted
[31] Garofalo A.M. *et al* 2009 *Phys. Plasmas* **16** 056119
[32] Callen J.D. *et al* 2009 *Nucl. Fusion* **49** 085021
[33] Greenfield C.M. *et al* 2001 *Phys. Rev. Lett.* **86** 4544
[34] Burrell K.H. *et al* 2001 *Phys. Plasmas* **8** 2153
[35] Garofalo A.M. *et al* 2011 Advances toward QH-mode viability for ELM-stable operation in ITER *Nucl. Fusion* submitted
[36] Burrell K.H. *et al* 2009 *Phys. Rev. Lett.* **102** 155003
[37] Pace D.C. *et al* 2011 *Nucl. Fusion* **51** 043012
[38] Tobias B. *et al* 2010 Fast ion induced shearing of Alfvén eigenmodes measured by 2D electron cyclotron emission imaging *Phys. Rev. Lett.* submitted
[39] Spong D.A. *et al* 1992 *Phys. Fluids* B **4** 3316
[40] White R.B. and Chance M.S. 1987 *Phys. Fluids* **27** 2455
[41] Snyder P.B., Groebner R.J., Leonard A.W., Osborne T.H. and Wilson H.R. 2009 *Phys. Plasmas* **16** 056118
[42] Snyder P.B. *et al* 2011 A first principles predictive model of the pedestal height and width: development, testing, and ITER optimization with the EPED model *Nucl. Fusion* submitted
[43] Yan Z. *et al* 2010 Pedestal turbulence dynamics in ELMing and ELM-free H-mode plasmas *Proc. 23rd IAEA Conf. on Fusion Energy (Daejeon, Republic of Korea, 11–16 October 2010)* paper EXC/P3-05 http://www-pub.iaea.org/MTCD/Meetings/PDFplus/2010/cn180/cn180_papers/exc_p3-05.pdf
[44] Osborne T.H. *et al* 2010 Scaling of H-mode pedestal and ELM characteristics in the JET and DIII-D tokamaks *Proc. 23rd IAEA Conf. on Fusion Energy (Daejeon, Republic of Korea, 11–16 October 2010)* paper EXC/2-1 http://www-pub.iaea.org/MTCD/Meetings/PDFplus/2010/cn180/cn180_papers/exc_2-1.pdf
[45] Beurskens M. *et al* 2010 H-Mode pedestal scaling in DIII-D, AUG and JET *Phys. Plasmas* submitted
[46] Snyder P.B., Wilson H.R. and Xu X.Q. 2005 *Phys. Plasmas* **12** 056115
[47] Schmitz O. *et al* 2010 Key results from the DIII-D/TEXTOR collaboration on the physics of stochastic boundaries projected to ELM control at ITER *Proc. 23rd IAEA Conf. on Fusion Energy (Daejeon, Republic of Korea, 11–16*

*October 2010)* paper EXP/P3-30 http://www-pub.iaea.org/MTCD/Meetings/PDFplus/2010/cn180/cn180_papers/exd_p3-30.pdf
[48] Hudson B. *et al* 2010 Transport and MHD analysis of ELM suppression in DIII-D hybrid plasmas using n=3 resonant magnetic perturbations *Proc. 23rd IAEA Conf. on Fusion Energy (Daejeon, Republic of Korea, 11–16 October 2010)* paper EXC/P5-02 http://www-pub.iaea.org/MTCD/Meetings/PDFplus/2010/cn180/cn180_papers/exc_p5-02.pdf
[49] Petrie T.W. *et al* 2011 Results from radiating divertor experiments with RMP ELM suppression *Nucl. Fusion* submitted
[50] Baylor L.R. *et al* 2010 ELM pacing by pellet injection on DIII-D and extrapolation to ITER *Proc. 37th EPS Conf. on Plasma Physics (Dublin, Ireland, 21–25 June 2010)* paper P2.117 http://ocs.ciemat.es/EPS2010PAP/pdf/P2.117.pdf
[51] Sovinec C.R. *et al* 2004 *J. Comput. Phys.* **195** 355
[52] Izzo V.A. *et al* 2010 Runaway electron modeling for rapid shutdown scenarios in DIII-D, Alcator C-Mod, and ITER *Nucl. Fusion* submitted
[53] Hollmann E.M. *et al* 2008 *Nucl. Fusion* **48** 115007
[54] Commaux N. *et al* 2011 Novel rapid shutdown strategies for runaway electron suppression in DIII-D *Nucl. Fusion* submitted
[55] Wesley J.C. *et al* 2008 Fast plasma shutdowns obtained with massive hydrogenic, noble and mixed-gas injection in DIII-D *Proc. 22nd IAEA Conf. on Fusion Energy (Geneva, Switzerland, 13–18 October 2008)* paper EX/7-3Rb http://www-pub.iaea.org/MTCD/Meetings/FEC2008/ex_7-3rb.pdf
[56] Allen S.L. *et al* 2010 Particle control and transport experiments in the DIII-D tokamak with graphite walls *Proc. 23rd IAEA Conf. on Fusion Energy (Daejeon, Republic of Korea, 11–16 October 2010)* paper EXD/6-4 http://www-pub.iaea.org/MTCD/Meetings/PDFplus/2010/cn180/cn180_papers/exd_6-4.pdf
[57] Gohil P. *et al* 2011 L-H transition studies on DIII-D to determine H-mode access for non-nuclear operational scenarios in ITER *Nucl. Fusion* submitted
[58] Gohil P. *et al* 2009 *Nucl. Fusion* **49** 115004
[59] Martin Y.R. *et al* 2008 *J. Phys.: Conf. Ser.* **123** 012033
[60] Schaffer M.J. *et al* 2011 ITER test blanket module error field simulation experiments at DIII-D *Nucl. Fusion* submitted
[61] Kramer G.J. *et al* 2010 Fast ion effects during test blanket module simulation experiments in DIII D *Proc. 23rd IAEA Conf. on Fusion Energy (Daejeon, Republic of Korea, 11–16 October 2010)* paper EXW/P7-10 http://www-pub.iaea.org/MTCD/Meetings/PDFplus/2010/cn180/cn180_papers/exw_p7-10.pdf
[62] Park J.-K. *et al* 2010 Robust correction of 3D error fields in tokamaks including ITER *Proc. 23rd IAEA Conf. on Fusion Energy (Daejeon, Republic of Korea, 11–16 October 2010)* paper EXS/P5-12 http://www-pub.iaea.org/MTCD/Meetings/PDFplus/2010/cn180/cn180_papers/exs_p5-12.pdf